Astron. Astrophys. 349, 301–311 (1999)

ASTRONOMY AND ASTROPHYSICS

Determination of horizontal velocity fields at the sun's surface with high spatial and temporal resolution

Th. Roudier[1], **M. Rieutord**[1], **J.M. Malherbe**[2], **and J. Vigneau**[1]

[1] Laboratoire d'Astrophysique de Toulouse, Observatoire Midi-Pyrénées, 14 avenue E. Belin, F-31400 Toulouse, France
[2] DASOP, Observatoire de Paris, Section de Meudon, F-92195 Meudon, France

Received 30 March 1999 / Accepted 14 June 1999

Abstract. We analyse the two algorithms which have been used in the past few years to determine the horizontal flow fields at the Sun's surface, namely the Local Correlation Tracking (LCT) of L. November and the Feature Tracking of L. Strous. Analysing the systematic errors introduced by LCT, we show that these errors come from the averaging processes. More precisely, they arise from the interpolating step of the algorithm: granules' motions determine the flow on an irregular grid which is then interpolated to derive quantities such as horizontal divergence or vertical vorticity. Interpolation is therefore a crucial step since mesoscale structures have mainly been studied through divergences and vorticities. We conclude that a reliable algorithm should be based on the tracking of coherent structures, like granules, since they are representative of the fluid motion, and should contain an interpolator which keeps track of the errors introduced either by location of the data (the shape of the irregular grid) or by the noise in the data.

Key words: Sun: atmosphere – Sun: general – Sun: granulation – Sun: photosphere

1. Introduction

The dynamical properties of the photosphere and the turbulent-convection scale hierarchy may be determined or constrained by measuring velocity fields at the sun's surface. The abundant observational evidence of mass motions inside the sun (*i.e.*, solar flows) indicates a large variety of types and scales of these flows. The associated velocity fields may be determined by two methods: (*i*) the measurement of the classical Doppler effect, which yields the velocity component along the line of sight; and (*ii*) the measurement of some tracers' displacements, which yields the horizontal flow. The combination of two such methods could in principle give access to the three components of the surface velocity field.

The Doppler measurements allow direct access to the mass motions in the photosphere but it is quite difficult to get a long time serie with high spatial resolution to follow the solar surface evolution, since spectroscopic or spectroimagery techniques are quite involved: they require recording line profiles in a two-dimensional field of view. In contrast, horizontal flows in the solar photosphere can be measured from solar granulation tracking by using the usual imagery (large bandwidth) techniques. Individual granules then act as tracers.

From the best mountain-top sites with good seeing, high resolution time series lasting several hours have been obtained (Muller et al. 1992, Simon et al. 1994). The use of tracers to determine solar horizontal flows implies making the assumption that we observe the horizontal motion of the plasma through the granules' motions. Indeed, the displacement of a bright feature may be due to other effects: heat diffusion, travelling waves, etc. The granule displacement is a combination of these effects with the proper motion of the plasma, but it is generally assumed that this latter effect is dominant and noised by the other processes. On this basis, we can consider the tracers' motions as a reasonable tool to study flow patterns such as mesogranulation and supergranulation which are presently associated with the main convective scales in the solar photosphere and chromosphere.

The determination of granule motion is, however, not a simple matter and today only two techniques have been developed by different groups: Local Correlation Tracking (LCT) by Shine and November (November 1986, November and Simon 1988, November 1989) and Feature Tracking (FT) by Strous (1994, 1995a).

However, the comparison of the results of these two techniques applied to the same set of data (Simon et al. 1995, Strous 1995b), shows discrepancies in the resulting velocity, divergence and vorticity fields. The disparity of the results is far from satisfactory and claims for more robust algorithms in order to discriminate real physical processes at the solar surface from effects due to data processing. For instance, it is not clear at all that the mesogranulation scale is a distinctive scale of convection (Straus and Bonaccini 1997) and not an artefact of data processing.

The aim of the present paper is to further investigate and improve the two techniques, and then compare their results when they are applied to the high resolution data collected at Pic du Midi, the idea being to get the highest spatial and temporal resolution for the horizontal velocity field. We can then use these data to get a detailed picture of the dynamics of convection in the photosphere.

Send offprint requests to: Th. Roudier

The paper has been organized as follows: In Sect. 2 we test the LCT algorithm on artificial data and show the systematic errors introduced. Sect. 3 is devoted to a presentation of our algorithm, christened CST for "Coherent Structures Tracking", and which is an improved version of Strous' Feature Tracking. We then discuss (Sect. 4) one of the main problems of these measurements, namely interpolation. In Sect. 5, using Pic du Midi data, we illustrate the application of the CST algorithm and present other tests on the LCT which we apply to binarized data. Conclusions are drawn in Sect. 6.

2. Local correlation technique

2.1. Principle

The LCT algorithm is based on the fact that if an "intensity pattern" is moved by the solar flow field, we may measure this flow field by maximizing the local correlation of two successive sub-images which are shifted with respect to each other. The shift which maximizes the correlation is taken as the true displacement of the pattern.

As shown by Darvann (1991), the LCT algorithm has been used by several authors to derive the horizontal velocity fields in different types of solar applications (e.g. Brandt et al. 1988, Title et al. 1989, Molowny Horas 1994, Wang et al. 1995, Kitai et al. 1997, Roudier et al. 1998, Ueno and Kitai 1998).

2.2. The precision of the LCT

The results of this algorithm, in terms of precision, were first tested by November and Simon (1988) through noise analysis. Using an 80 mn image sequence, these authors estimated that mean velocities could be evaluated with a precision as high as 20 m/s. These first results were seemingly very optimistic; indeed, the advent of a new method, namely Feature Tracking, promoted by Strous (1994, 1995a), prompted Simon et al. (1995) and Strous (1995b) to make a comparison between the two algorithms and the results have been particularly worrying, shedding doubts on all previous measurements based on LCT. The disagreement between the two methods especially affects the flow fields of moderate or low intensities and, above all, the velocity gradients such as divergences or vorticities.

Considering the complexity of the data processing it is not too surprising that discrepancies appear between different algorithms. It is more surprising, however, that an algorithm such as LCT was never tested (to our knowledge) on artificial data and its ability at restoring a given velocity field never shown. This is the reason why we generated an artificial data set where granules are replaced by intensity patterns in the form of ellipses or rectangles as shown in Fig. 1. These patterns move as solid bodies in a pure translational motion; no distortion is introduced.

We thus make two plates and apply the LCT algorithm to restitute the initial velocity field. From the result displayed in Fig. 2, it is clear that, if one recognizes the original flow, some noise or systematic errors (with 25% rms amplitude) are introduced by the processing, while the Coherent Structures Tracking algorithm gives back the original data.

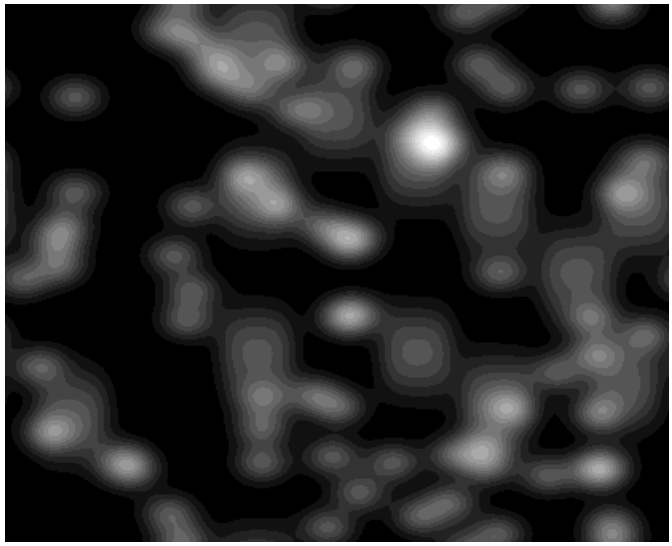

Fig. 1. The artificial image used for testing LCT.

3. Coherent structures tracking

3.1. Principle

Feature Tracking (FT) is another algorithm first applied to solar data by Strous (1994,1995a). The idea is to assume granules are objects advected by an underlying flow which we wish to measure. Of course, these tracers are not like aluminium flakes in fluid mechanics experiments: they are not passive scalars but rather (thermally) coherent structures of turbulent convection; their contour is not precisely defined and their lifetime is short. Despite these inconveniences, and provided we can define the granule in a unique way, this method is certainly more reliable at evaluating a horizontal velocity than the previously described LCT.

The reason to assert such a statement relies on the physical nature of granules. Their horizontal scale indeed represents the smallest scale whose motion is almost entirely due to advection. It is a thermally coherent structure which naturally defines the scale below which it is useless to measure a velocity from isophot motion. From this point of view, it is clear that LCT does not measure the motion of coherent structures as, for instance, when the gaussian window comprises an intergranule lane and parts of adjacent granules. It is therefore tempting, with this technique, to over-resolve the data and generate meaningless results.

The Coherent Structure Tracking (CST) algorithm, to be described below, is an improved version of the one already used by Strous (1995a). Our improvements may be summarized as follows: before determining the zero-curvature contour which defines the granule we first filter the image with a gaussian window which has the effect of removing some noise; once the contour (and therefore the granule) is defined, we make the segmentation; through opening operations, we further break narrow isthmuses and remove thin protusions; finally, we eliminate all granules which deform too much. The motion of granules is pinpointed by that of the barycenter of the surface enclosed by

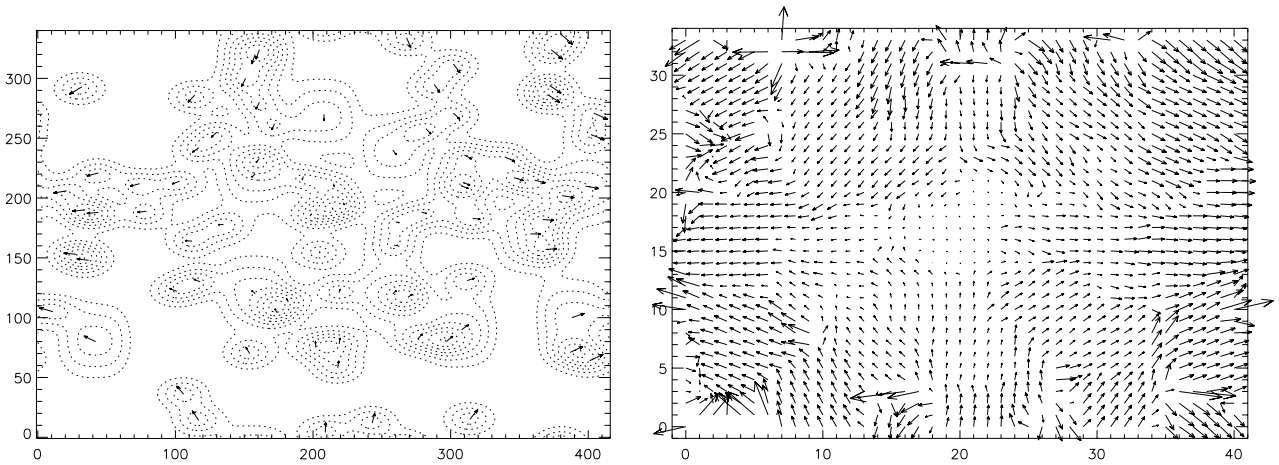

Fig. 2. The original flow is simply $V_x = K(x - 208)$ and $V_y = -K(y - 170)$. In the left-hand plot we show the sampling given by the randomly distributed patterns of Fig. 1. The right-hand plot shows its restoration by the LCT algorithm using a 10 pixel gaussian window. The flow is qualitatively restored, but large errors appear here and there. The application of the CST to the original flow gives back the data on the left-hand plot. Axis units are in pixels (left) and tens of pixel (right).

the contour, while Strous (1994) tracks the intensity maximum enclosed by the contour. We think that, in this way, tracking is more robust, as it is not sensitive to intensity fluctuations inside granules and represents more faithfully the mean displacement of these coherent structures.

3.2. Cleaning the data: destretching and filtering

Before starting the CST algorithm, it is necessary to clean up the images in order to remove, as much as possible, the "motions" due either to atmospheric seeing, instrumental distortion or acoustic solar waves. This is done through three operations, which are rigid alignment, destretching, and subfundamental $k - \omega$ filtering.

The most critical point of this processing chain is the destretching, which has the delicate task of removing effects of atmospheric seeing and instrumental distortions. We shall therefore discuss somewhat the error which is generated by this operation. For this purpose we use a set of seven images taken every 50 ms with an exposure time of 2 ms[1]. For this sequence the solar signal is identical and variations are only due to seeing effects.

These seven images are rigidly aligned and destretched. The segmentation (see Sect. 3.3 for a description) is then applied and a 'virtual' displacement is measured. This gives an estimation of the noise left by these two operations. An example of two different images of this short sequence, after destretching and segmentation, is shown in Fig. 3.

Over 409 total granules detected in an image, only 15 to 20 ($\sim$5%) appear segmented in a different way. However, during the whole burst, we could track $\sim$95% of the granules because, in general, the failing of segmentation occurs on the same granules. Hence, a consequence of distortions, is that some tracers are lost during the processing of a long time-sequence.

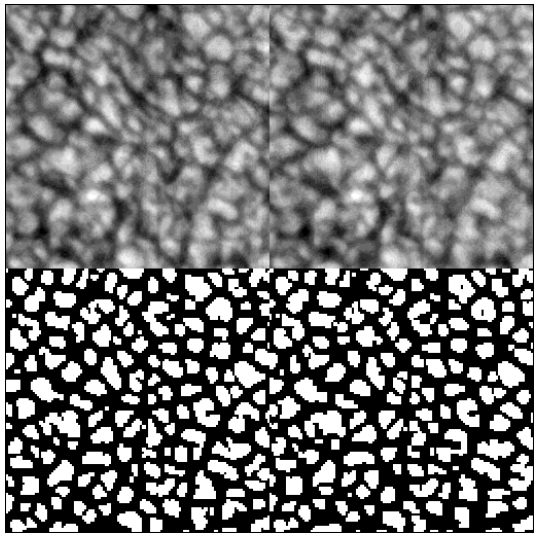

Fig. 3. Two (magnified) images from the burst of seven images taken at Pic du Midi on 20 September 1988; the pixel size is 75 km. Differences between these two images (and between their segmented counterpart) are only due to the atmospheric seeing.

From the seven destretched frames, the displacement of each granule was measured; the result is drawn in Fig. 4. The distribution is peaked around 15 km which corresponds in this case to 0.2 pixel (1 pixel = 75 km). This is much below the spatial resolution of the images, which is 2.4 pixels. This shows that even if the frontiers of granules are blurred by the spatial resolution of the instrument, the positions of the barycenters of granules can be measured precisely, as is well known in astrometry.

If we consider that the seeing introduces a virtual displacement of 0.2 pixel in the position of the barycenter of the granules, the velocity of a granule lasting 160 s will be spoilt by an er-

[1] These images are from the same film as those described in Sect. 5, except that the pixel size is slightly smaller (75 km instead of 101 km).

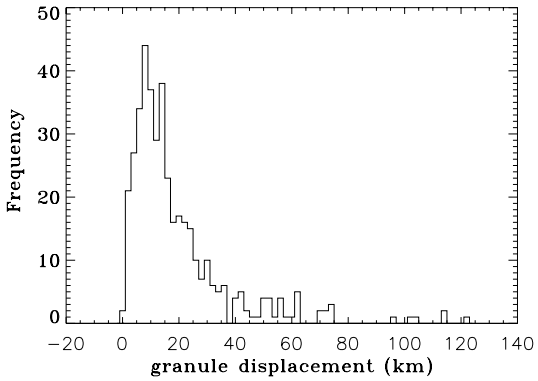

Fig. 4. A histogram of granules' motions due to seeing effects.

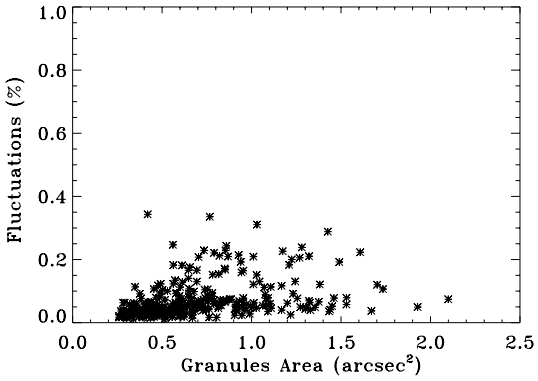

Fig. 5. Percentage of variation of the area of granules produced by seeing effects.

ror of 130 m/s (the pixel's size now being 101 km). This is of course an order of magnitude which corresponds to a rather high resolution in time.

For all the granules, we also measured the variations of their area. This is represented in Fig. 5 where we displayed the percentage of variation as a function of the area. The mean variation is around 11%, which is consistent with the positioning error on the center of gravity.

We therefore see that some seeing effects are left after the destreching and alignment operations. However, this error is acceptable since most of the granules are showing velocities in the range 350 m/s–1 km/s (see below).

3.3. Segmentation

The next step is the segmentation; *i.e.*, the transformation of the intensity map into a binary map. This transformation is crucial as it defines the objects whose motions are then measured. The difficulty here is to find a criterion which defines the object. A simple one is to use a threshold in intensity above which a granule is said to exist. However, such a criterion does not work properly if the intensity shows variations at scales larger than the objects. After different tests, it appears that the criterion of Strous gives the best results.

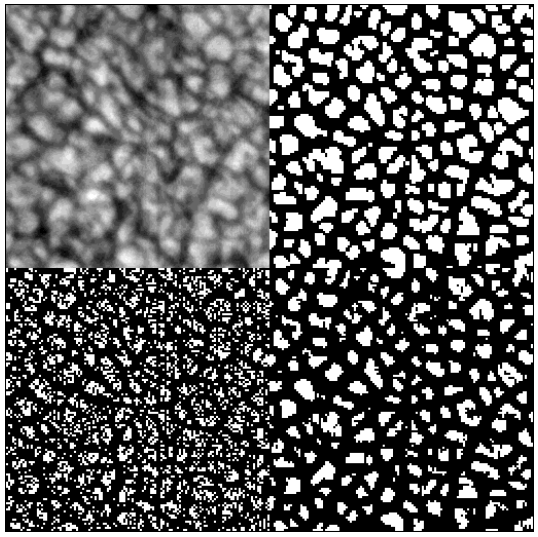

Fig. 6. An illustration of the effects of the convolution and opening operations on the segmentation. The upper-left plot is the original image. The lower-left is the segmentation of the image. The lower-right shows the result of segmentation after a convolution of the image by a $1''$ gaussian window. The upper-right plot is the result obtained after opening operations on the lower-right picture. Note that this is the same field as that of Fig. 3.

This criterion uses the intensity of three adjacent pixels, I_1, I_2, I_3 say, to define a local curvature of the intensity field a as

$$a = I_1 - 2I_2 + I_3$$

This quantity is computed in four directions (x, y and diagonal axis) to get a result invariant under rotations. When the second spatial derivatives have the same sign in the four directions, for example negative, the pixel belongs to a bright object, in the opposite case it belongs to the dark intergranule.

However, before doing this segmentation we convolve each frame with a gaussian window whose size depends on the pixel's size in arcsec; in general, we used a window size between 3 and 7 pixels. This smoothing reduces the noise and therefore improves the computation of a. In addition, we improve the segmentation of the different objects present in the field of view by applying a classical opening operation which breaks narrow isthmuses and eliminates thin protrusions. This procedure is illustrated in Fig. 6.

This segmentation method, which depends only on the location of the "zero-curvature" intensity field, is local and independent of the intensity amplitude (Strous, 1995a).

3.4. Labeling (2D)

Once segmentation is performed, objects are born and need to be labelled in order that we can follow their evolution.

The labeling of each bright object in an image is performed by using an automatic algorithm which follows the perimeter of the detected object. Then all the points which are located inside the external perimeter and which are also detected as bright

elements are labeled with the same object number. Our labeling method differs from the one of Strous in that we do not consider as members of the same object those pixels which only share a common vertex.

Once the objects are defined and labelled, we need to define a point whose motion will best represent their motion. Since our objects are in fact polygons with no features inside, the appropriate point is simply the barycenter of the (constant surface density) polygon. Its position can be computed from the points defining its boundary; for a n-points polygon, it is

$$X_g = \frac{1}{3}\frac{\sum_{i=1}^{n}(x_i^2 + x_i x_{i+1} + x_{i+1}^2)(y_{i+1} - y_i)}{\sum_{i=1}^{n}(x_i y_{i+1} - x_{i+1} y_i)}$$

$$Y_g = \frac{1}{3}\frac{\sum_{i=1}^{n}(y_i^2 + y_i y_{i+1} + y_{i+1}^2)(x_i - x_{i+1})}{\sum_{i=1}^{n}(x_i y_{i+1} - x_{i+1} y_i)}$$

The derivations of these formulae are given in the appendix.

The horizontal flow velocities are determined from the displacements of the barycenter of the objects, which keep the same label during time evolution (see below). Let us note that here too our method differs from the one of Strous, who follows the maxima of intensity. We believe that our method is more reliable since it is not sensitive to intensity variations inside a granule.

3.5. Time identification (3D)

The next step consists in identifying the trajectories of barycenters for the whole time sequence. This step is complicated by the fact that granules are not passive tracers of a horizontal flow. Their shape changes during their lifetime and it is well known that it is quite difficult to define the life history of a typical granule. Hence, splitting into multiple objects, merging of objects, and disappearances or appearances between two successive images have all to be taken into account.

To circumvent this difficulty, we chose to track only the most coherent objects (*i.e.*, granules) whose deformation remains below a given level. For this purpose, we use the ratio $f = P^2/A$, where P is the perimeter and A the area of the object. This ratio measures the shape of the object and has actually been used to determine the fractal dimension of granules (Roudier and Muller 1986). We use this ratio to fix a threshold of the deformation rate. When an object experiences a change of shape greater than this threshold, it is considered as a new object which is tracked independently of the previous one. In this way we filter out motions of barycenters which are due to deformations of granules.

Finally, another criterion is also necessary to determine the trajectories of barycenters. From one frame to the next we do not allow the displacement to be larger than one pixel. This is, however, specific to our data, for the spatial resolution is $0.14''$/pixel and two successive frames are separated by 20 s; a one-pixel displacement is equivalent to a velocity of 5 km/s, which is quite large.

When these two criteria are met, objects are labeled from one frame to the next with the same number; otherwise, the number is changed to a new one.

Hence, we construct a bunch of trajectories which non-uniformly sample the field of view.

3.6. Time-averaging

The determination of velocities requires, however, that we define a time interval after which we measure the displacement. This time interval should be as short as possible for the best time resolution, but long enough so that the displacement exceeds the spatial resolution. Hence, the smallest measurable velocity is given by the spatial resolution divided by the time interval. Sacrificing time resolution, we may detect very low velocities, but we should not be too demanding about the precision of those velocities; as we shall see below, some systematic errors are introduced by the velocity field reconstruction (the interpolation for short). If we wish to detect true motions among the noise of errors, the velocities should be high enough. The shortest time interval is therefore given by

$$T = \frac{\delta x}{\delta v} \tag{1}$$

where δx is the precision on the location of a coherent structure and δv is the noise level introduced by the algorithm. Time windows larger than T may detect lower velocities but uncertainties may be larger than the signal.

At this point it is worth underlining the danger of using a sliding window. One may be tempted to use a rather large temporal window, for getting a greater precision on the velocity, but to shift this window by a time step smaller than the width of the window. Such an operation gives a higher sampling of the signal but the information is not independent; in fact, one is just computing the convolution of the true signal with the window. A consequence of this procedure when combined with a spatial window, is to give the illusion that a phenomenon is continuous in time while it is not; for instance, it may generate long-lived structures from random appearances of short-lived structures.

Finally, let us discuss the question of the use of a given time sampling. The ideal one would be, for a ground based observation, series of bursts of images such as the one described in Sect. 3.2. Each burst should contain many images so as to evaluate seeing effects and should be separated from the next burst by a time interval optimized for keeping track of the most rapidly evolving granules. Each of these time intervals would give one value of the velocity per granule.

4. Field reconstruction

Now comes what is certainly the most delicate point of the data processing: namely, the recontruction of the velocity field as a continuous function of space (and eventually time), and the evaluation of its derivatives (*i.e.*, the horizontal divergence and vertical vorticity).

This reconstruction is a well-known and difficult problem of data processing: using a random sampling of a continuous function (the data), how can we reconstruct the function introducing a minimum of new information? Then, once the function is re-

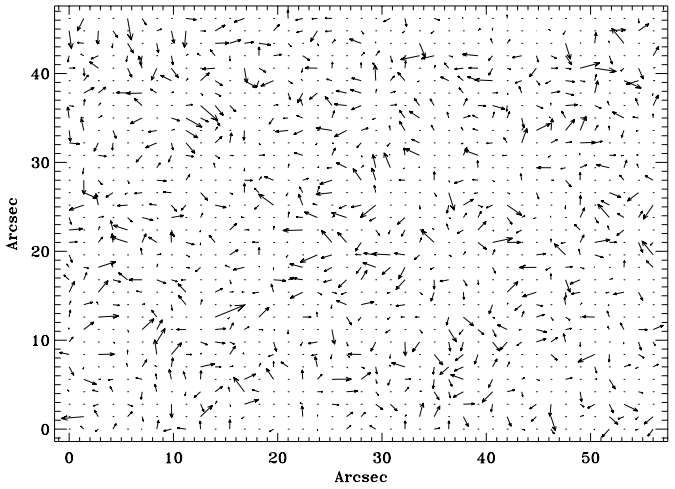

Fig. 7. Velocity field determined by CST with a temporal window of 10 mn.

constructed, how can we estimate the local uncertainty of the results introduced either by the method or by the noise of the data? These are the basic questions that need to be answered. Techniques already exist in the field of signal processing (Torrence and Compo 1998), but they have been developed essentially for one-dimensional data. Their generalization to two-dimensional data sets, although not straightforward, is possible and will be presented in a forthcoming paper.

4.1. Using the CST data

CST data have the peculiarity of being a sampling of the velocity field on an irregular grid. However, each measure of the velocity components can be completed by the size of the structure used to make the measurement. Thus, for each point where the velocity is measured, we also know its smallest scale. This information can be used to reconstruct the field; however, in this paper, we will content ourselves with a more expedient method: dividing the field into boxes 1.4″ wide, we simply take the average of the values of the horizontal velocity which fall in the box and thus reconstruct a coarse-grid velocity field. The coarseness of the grid increases with the lack of data. If the grid is too fine with respect to the data, some points are devoid of data as in Fig. 7.

Once the velocity field is known, we derive the divergence using simple differences between neighbouring points.

4.2. Using LCT$_{bin}$ data

Another way of obtaining a gridded velocity field is to use the Local Correlation Tracking in spite of the inconveniences mentioned above (Sect. 2.2).

LCT indeed gives a uniformly sampled velocity field and immediately produces "interpolated data". However, the problem is to know what is represented by these data; *i.e.*, how far can we trust the velocity field obtained. We do not have the answer to this question, unfortunately, but we noticed that the results can be improved if LCT is applied to binarized data after segmentation; we shall refer to this version of LCT as LCT$_{\rm bin}$. In this way, the internal intensity fluctuations, which may be residues of seeing or of 5 min-oscillations, are removed and one of the known problems of LCT, namely sensitivity to large gradients, is eliminated. Some noise, classically attributed to granular motion and which appears when the window is large (2–3″) (Darvann 1991), is also reduced.

LCT$_{\rm bin}$, however, needs an extraparameter which is the size of the gaussian window. Its size should be chosen according to Shannon's criterion; since granules are constraining the sampling of data, the window size should be half of the granules' mean size, which is around 1.4″ according to Roudier and Muller (1986). We therefore choose a window size of 0.7″ (5 pixels).

Using this spatial sampling, it turns out that we can use a temporal window as short as five minutes which is useful to follow the time evolution of the velocity field in parallel with the evolution of the granules.

5. Application to the Pic du Midi data set

5.1. The data set

As a test we now apply the foregoing algorithm to a data set composed of 540 images obtained at Pic du Midi on 20 September 1988, covering an area of 58″ × 48″ (42000 × 35000 km^2); the time interval between two successive frames is 20 s and the whole sequence lasts three hours. The spatial resolution of the instrument is 0.25″ and the pixel size is 0.14″.

These images were rigidly aligned and destretched to remove atmospheric distortions. The subfundamental filter was then applied to remove brightness variations due to the 5 minute p-mode oscillations. Images were segmented and objects labeled. However, before determining the granules displacements, we need to specify the threshold of the deformation rate which we use to select "good" granules.

For this purpose, we use the statistical relation between the perimeter and the area of a granule, $P \propto A^{D/2}$ where D is the fractal dimension, first measured by Roudier and Muller (1986), the value of which is $D \approx 1.25$ for granules smaller than 1000 km. Hence, the shape parameter $f = P^2/A$ should behave as $A^{0.25}$.

According to this statistical relation, we may now evaluate the mean deformation of a granule between two successive plates (*i.e.*, after 20 s of evolution). As a typical velocity of expansion is 2 km/s (Brandt et al. 1991), after 20 s of evolution the size of a granule has increased by 80 km typically. The shape parameter of a granule of diameter L has therefore increased by a factor $(1 + 80/L)^{0.5}$ if L is expressed in km. The smallest (visible) granules have a typical diameter of 200 km and therefore experience a typical deformation of 18.3% while for larger ones, with a horizontal size of 1000 km, f varies only by 4%.

This estimation gives a good range where the shape changes can be selected in order to keep track of coherent objects whose proper motions are less perturbed by shape variations. In practice, a careful check on a large sample of granules shows that the value 18% is convenient to keep a lot of granules in the se-

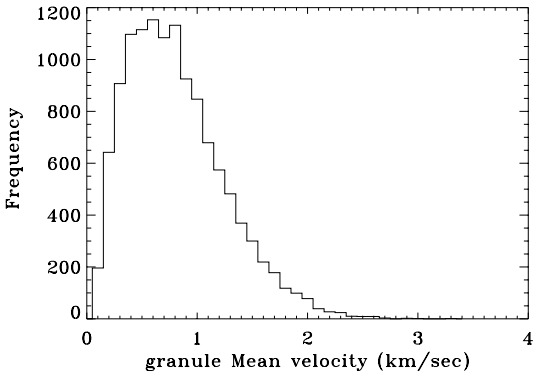

Fig. 8. Histogram of granules' mean velocities.

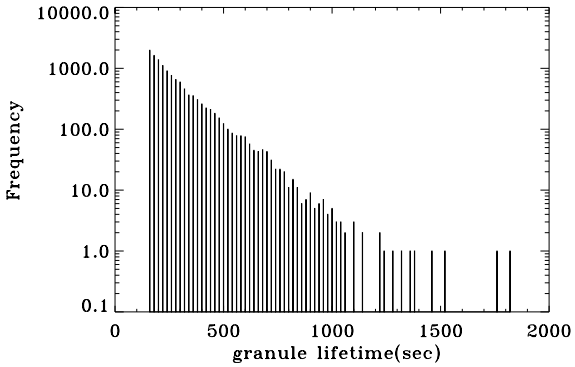

Fig. 9. Lifetime of tracked granules derived from the Pic du Midi data set. The mean lifetime is around 140 s.

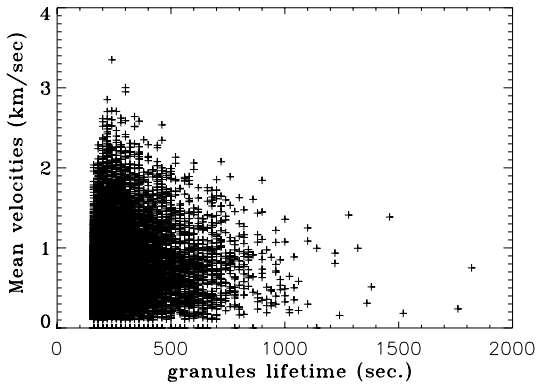

Fig. 10. Distribution of mean velocities of granules as a function of their lifetime.

quence and at the same time to avoid the merging and splitting cases. By using such a threshold, some large granule evolutions are lost because of large deformation rates, but our experience shows that the number of such granules is acceptable.

During this 3h sequence, 12509 "granules" (our coherent structures), with a minimum lifetime of 160 sec, and a rate of deformation less than 18%, have been found. This is a small fraction (12%) of all the granules detected; hence, the improvement of the quality of the measure is paid for by a high rejection rate of granules. However, an improvement of the spatial resolution would remove part of this constraint: short-lived granules could be included and would sample the field of view more densely.

5.2. Some statistical by-products

During the processing of data some by-products can be obtained, especially statistical distributions. These are essentially histograms of granule lifetime or granule mean velocities.

The granule velocity histogram, shown in Fig. 8, is peaked around 0.6 km/s with a distribution reaching up to 3 km/s; the cutoff at 0.3 km/s is due to the spatial resolution. The majority of velocities are located below 1.5 km/s.

The granule lifetime histogram (Fig. 9), derived from our measurements, reveals an exponentially decreasing distribution from 160 s (our fixed minimum) up to 1000 s. The fit of the exponential reveals a mean lifetime of $\sim$140 s which is somewhat smaller than 150 s-300 s which was found in Title et al. (1989) using SOUP data or the 5.9-8.3 min found by Mehltretter (1978). We think that our shorter lifetime is due both to the higher resolution of our data (we include a larger number of small granules) and to the introduction of a threshold of deformation in the tracking of granules. Following this latter argument, we may say that this time (140 s) is a coherence time scale rather than a lifetime.

In Fig. 10 we combine data from the two preceding histograms into a single one which shows the tendency of fast moving granules to be short-lived while long-lived ones tend to move slowly.

5.3. Averaging

In order to illustrate the difficulties posed by flow field reconstruction and averaging processes, we shall use in various ways the results produced by the $\mathrm{LCT}_{\mathrm{bin}}$ algorithm.

We first concentrate on spatial averaging. As we argued in Sect. 4.2, we use a spatial sampling of $0.7''$ to derive the first view of the flow during the first 15 mn (Fig. 11 top). We then average this flow on square boxes of width $2.8''$ (Fig. 11 bottom) and compared it with the one derived directly from $\mathrm{LCT}_{\mathrm{bin}}$ using a gaussian window of $2.8''$ (Fig. 11 middle). These three figures clearly illustrate the effects of averaging. More quantitatively, taking the difference between the two averaged fields (with $2.8''$ windows) gives an order of magnitude for the effects. In this example, we find a residual velocity field randomly distributed with a rms amplitude of 130 m/s (local discrepancies may reach 400 m/s, however).

This example shows that spatial averaging at a resolution of $2.8''$ introduces systematic errors with an amplitude of 130 m/s. In principle, the time window of 15 mn yields a precision of 20km/900s = 22 m/s which is much below the above mentioned error. The temporal window should be reduced to (20 km)/(130 m/s) = 160 s. However, we found it safer, in order not to accumulate errors, to choose a time window somewhat larger than this; we take 300 s (5 mn).

We may now compare the mean of three velocity fields measured with the 5 mn temporal windows (Fig. 12) and the velocity field obtained using a 15 mn temporal window (Fig. 11 top). The results are quite different: the differences between the two fields

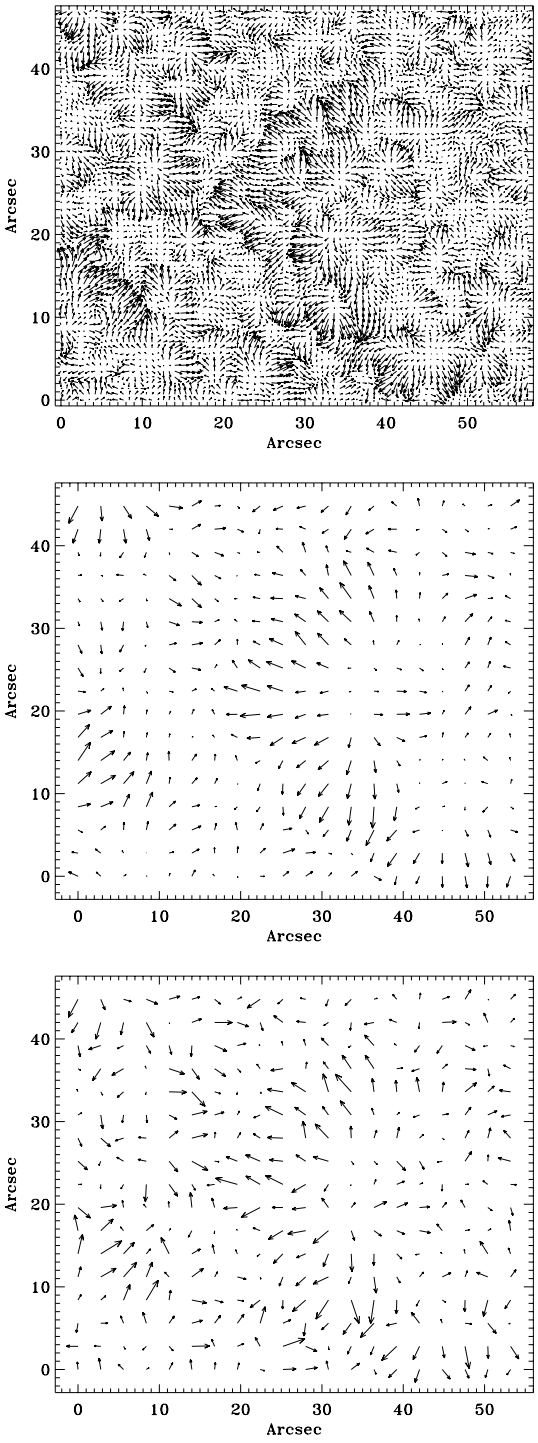

Fig. 11. *Top:* Velocity field determined by $\mathrm{LCT_{bin}}$ using a $0.7''$ gaussian window with a temporal window of 15 mn. *Middle:* Same as top but with a $2.8''$ gaussian window. *Bottom:* Mean velocity field obtained by averaging the flow in (top) over a square box of size $2.8''$. Note the difference between this latter flow field and the one yielded by the use of a $2.8''$ gaussian window.

show an rms error of 240 m/s; this also corresponds to a linear correlation between the two fields of 0.75 (see below).

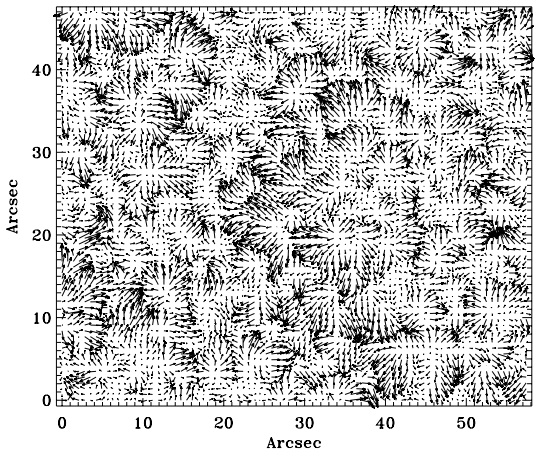

Fig. 12. The time interval (15 mn) used to compute Fig. 11 (top) is now divided in three windows of 5 mn which are used to determine three new velocity fields. The average of these three velocity fields is now plotted and should be similar to the one in Fig. 11 (top).

These two examples clearly show how important the averaging process is in the resulting velocity fields.

5.4. Comparison of flow maps derived by various techniques

To further appreciate the problems of the different algorithms, it is useful to compare their results for a subset of the data. We therefore compare the results of LCT and CST algorithms as well as one variation on each of them. Indeed, we modified the CST algorithm so as to make it similar as Strous'one as described in Strous (1995a); hence, we evaluate the influence of his "simple strategy" where no selection of granules and no opening operations are done. We shall refer to this algorithm as FT_S. We also consider the variant of LCT, namely $\mathrm{LCT_{bin}}$, described above. Hence, four algorithms are compared.

A first indication of the similarity of the results may be obtained by computing their linear correlation (here written for V_x)

$$C_x = \frac{\sum_{i=1}^{N} \left(V_x^i(1) - \langle V_x(1)\rangle\right)\left(V_x^i(2) - \langle V_x(2)\rangle\right)}{\sqrt{\left(\sum_{i=1}^{N}(V_x^i(1))^2\right)\left(\sum_{i=1}^{N}(V_x^i(2))^2\right)}}$$

where i is the index of pixels. Note that before computing this quantity each algorithm must be tuned so as to produce the same spatial resolution. Using the first 30mn of the time sequence, we obtain the velocity field shown in Fig. 13 and the corresponding divergence. Table 1 shows the correlation using a spatial window of $2.8''$.

The correlation between the different methods is around 0.75 which is almost the same as the one found when comparing different ways of averaging. These correlation coefficient again show the systematic errors introduced by the algorithms.

The rather high value of the correlation means that the main features of the velocity field persist from one method to the other. A visual inspection of the different results shows that, indeed, velocity fields are quite similar qualitatively. Moreover,

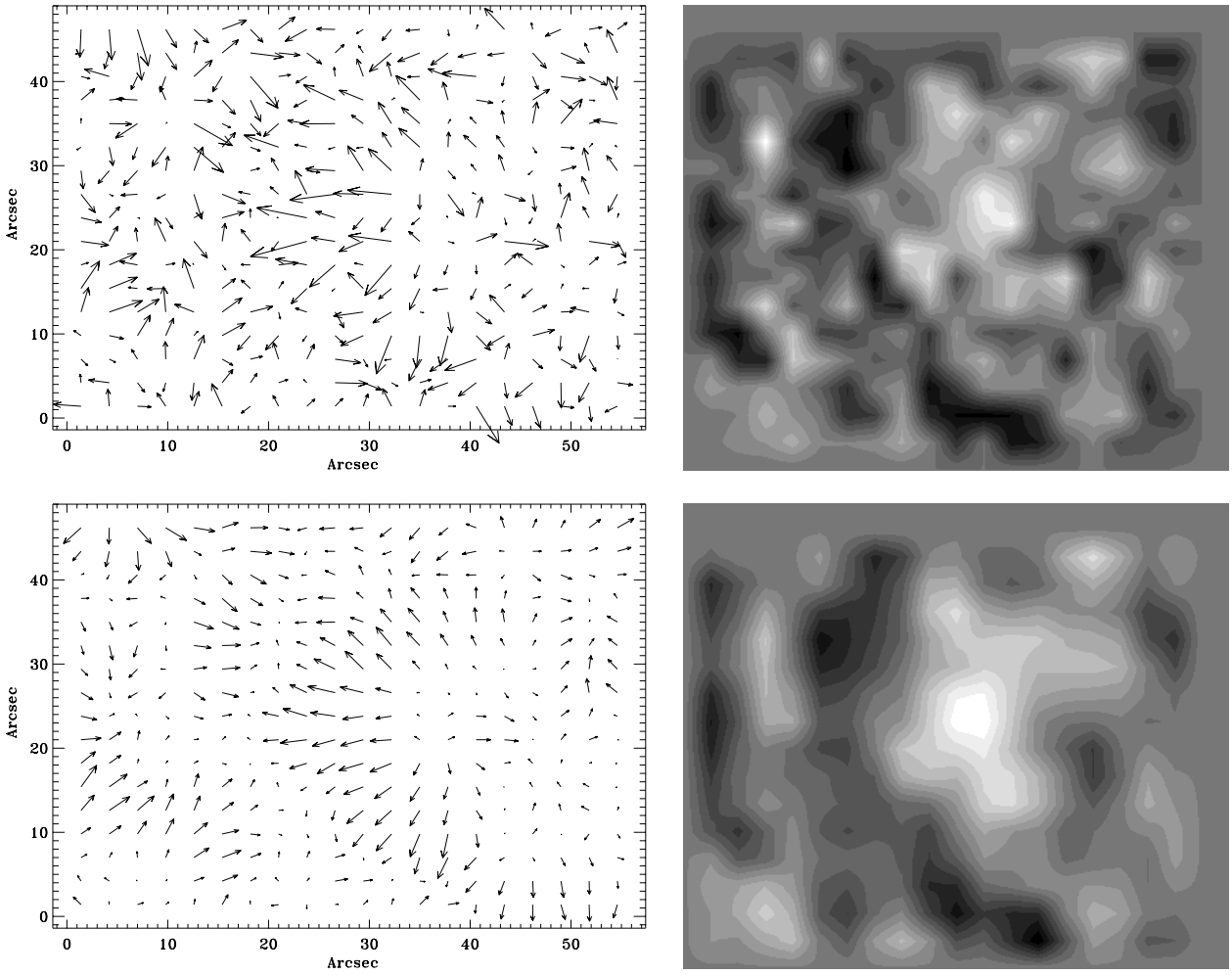

Fig. 13. Velocity field (left) and divergence field (right) obtained using the CST algorithm (top) or LCT algorithm (bottom). Data are time-averaged over 30 mn. One question raised by such plots is, how confident can we be in the reality of the structures shown in these figures?

Table 1. Correlation of the velocity fields computed by the different algorithms for the first 30 mn. Note that the correlations of $\mathrm{LCT_{bin}}$ with CST or FT_S is always higher than LCT's, thus showing the slight improvement gained with $\mathrm{LCT_{bin}}$.

	LCT	$\mathrm{LCT_{bin}}$	CST	FT_S
LCT	1	0.98	0.74	0.76
$\mathrm{LCT_{bin}}$		1	0.76	0.80
CST			1	0.87
FT_S				1

Table 2. Minima (m) and maxima (M) of the velocities (in km/s) and divergence (in s^{-1}) calculated from various methods for the first 30 min window of the 3-hour sequence all over the field of view. Note the reduced amplitude of the LCT results.

	V_x^m	V_x^M	V_y^m	V_y^M	Div_m	Div_M
GT	-1.49	1.10	-1.2	0.93	-4.6×10^{-4}	5.8×10^{-4}
GT_S	-1.50	1.01	-1.14	1.28	-4.8×10^{-4}	5.6×10^{-4}
LCT	-0.68	0.53	-0.71	0.64	-3.2×10^{-4}	3.3×10^{-4}

our comparisons seem to give a better similarity between the different outputs than the comparison shown in Fig. 1 of Simon et al. (1995). We suspect that part of the disagreement they found is due to the slight difference in the window sizes which have been used.

Another point, already noticed in previous comparisons (Simon et al. 1995 or Roudier et al. 1998), is the tendency of LCT to smooth the velocity fields. This tendency also appears in our results as shown by the values of the extrema of the fields (see Table 2).

6. Conclusion

In this paper we have tested, compared, and tried to improve (somewhat) the existing algorithms for measurements of horizontal flows at the sun's surface. We have shown how delicate the processing of these data is and how much care is needed in the averaging process in order to avoid systematic errors.

Our conclusion is that tracking coherent structures using segmentation with the criterion of Strous is certainly the most reliable measure of displacement, since the barycenter of binarized structures is measured precisely ($0.028''$). However, the

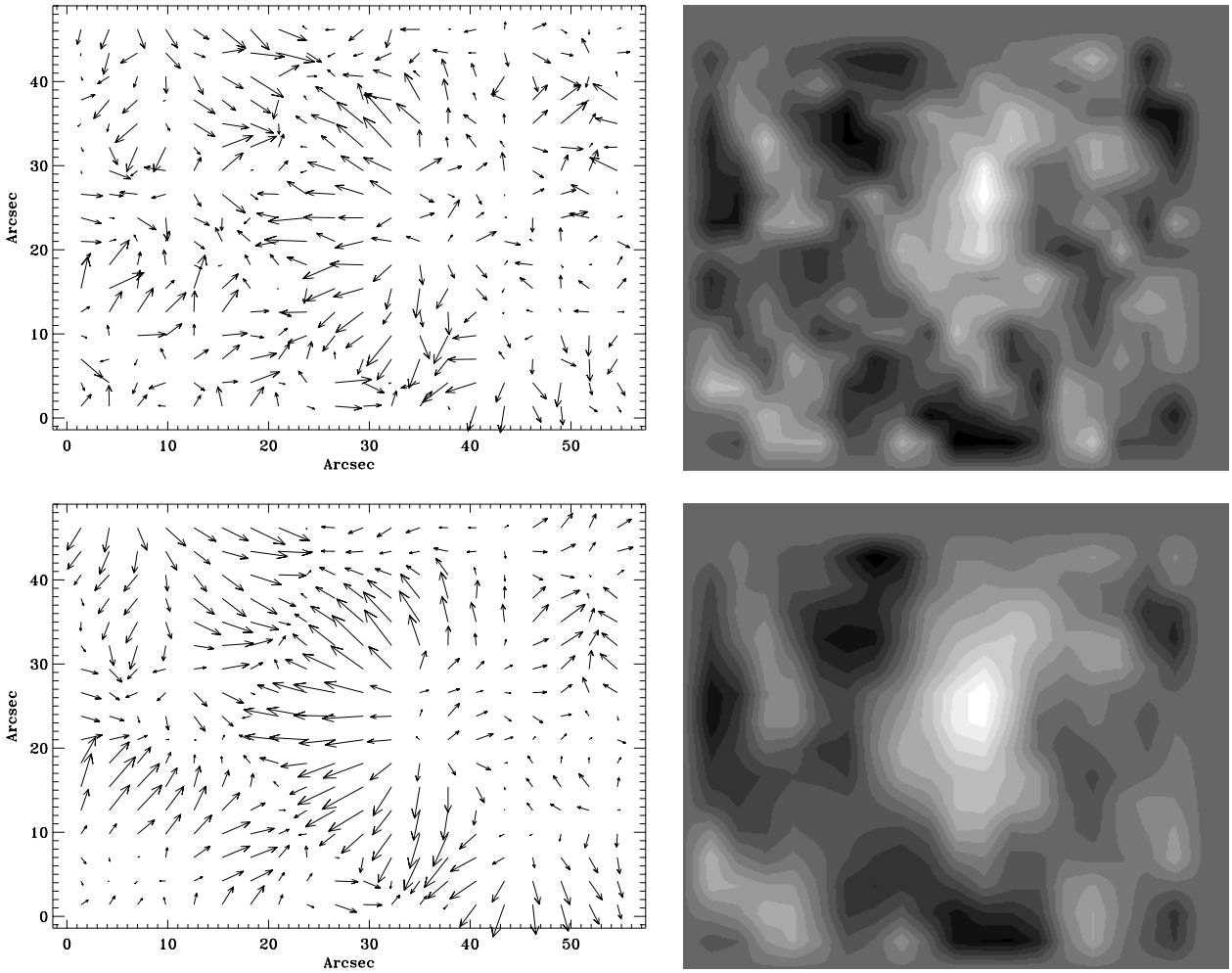

Fig. 14. Same as Fig. 13 but averaging the results over the total length of the sequence (three hours). Note the reduction of the scale structures when the algorithm changes from LCT to CST.

measurement of the displacement is only the first step towards the modelling of the surface flow of the sun and the identification of the important scales. The other important step is the reconstruction of the continuous velocity field which can then be used for further manipulations like spatial filtering, averaging, differentiation, etc. For these operations to give sensible results, we need to keep track of the local error introduced either by the method or the noise of the data. Therefore, it appears that it is necessary to devise a good interpolation of the data (*i.e.*, granules' displacements) which non-uniformly sample the field of view. At the moment, such an interpolator, which also yields the uncertainties on the results, does not exist. But a promising way lies in the use of wavelet analysis; such a tool is now under development and will be presented in a forthcoming paper.

Lacking this last and important part of the algorithm, we replaced it by an expedient which is either LCT or an average on a coarse grid. The comparison of the two results offers an estimate of the errors introduced by the two methods. However, we did not use LCT in a standard way: we applied this algorithm to the binarized data, respecting Shannon's criterion as far as possible. Actually, this enabled us to increase the time sampling to a five-minute step, which is a rather high temporal resolution compared to previous works which used at least a twenty-minute step. Such a time sampling is useful to follow the simultaneous evolution of the velocity field and the intensity patterns (granules).

From our results, it is clear that LCT gives good qualitative results and that salient features remain, regardless of the way data are manipulated. However, it is also clear that on the quantitative side, LCT introduces uncontrolled systematic errors which we estimate, using Pic du Midi data for example, around 200 m/s rms.

Finally, we note that the CST algorithm rejects a lot of granules: those which either deform too much or do not live long enough. Therefore, data points are not very dense in the field and the velocity field is not strongly constrained. This drawback may disappear partially when high resolution (less than $0.1''$) data are available. In such a case, short-lived granules may also be used and they are much more numerous. At the moment, with the present resolution, we should concentrate on long time-series of large fields which may be used to constrain the large-scale dynamics (like the supergranular scale).

The preceding critical review of the presently available algorithms for horizontal flow determination makes us fear that mesogranulation, which was described during the last ten years as another scale of solar convection, could be a by-product of systematic errors introduced by the wild application of LCT to solar images. Indeed, much of the detection of mesogranules is based on divergence measurements (e.g., November and Simon 1988, Muller et al. 1992, Roudier et al. 1998) which are quite sensitive to the way the velocity field is reconstructed. We shall come back to this question and that of supergranulation in a companion paper.

Acknowledgements. We are very grateful to Richard Muller for providing us with the three-hour sequence of Pic du Midi and to Laurence November for letting us use his LCT program. We are also very grateful to Gary Henderson for his careful reading of the manuscript. We acknowledge many fruitful discussions with Sylvie Roques.

Appendix

These formulae are obtained from the definition of the barycenter of a surface of constant density

$$X_g = \frac{\int\int_{(S)} x dx dy}{S} \quad \text{and} \quad Y_g = \frac{\int\int_{(S)} y dx dy}{S}$$

$S = \int_{(S)} dx dy$ is the area of the polygon. If we note that $2\pi \int_{(S)} x dx dy$ is in fact the volume of the torus generated by rotating S around the y-axis, and if we denote this volume by $\mathcal{V}_y$ then

$$X_g = \frac{\mathcal{V}_y}{2\pi S} \quad \text{and} \quad Y_g = \frac{\mathcal{V}_x}{2\pi S}$$

a result which is known as Guldin's theorem (Pérez 1997).

To compute the volume of a torus with a polygonal cross-section we first compute the volume of a thick disk whose edge is defined by the segment $\overline{A_n A_{n+1}}$ of two consecutive points of the polygon. Denoting (x_n, y_n) the coordinates of the n$^{\text{th}}$-point, the volume of the disk is simply

$$V_n = \frac{\pi}{3}\left(x_n^2 + x_n x_{n+1} + x_{n+1}^2\right)(y_{n+1} - y_n)$$

We note that the volume is positive (or negative) if $y_{n+1} > y_n$ (or $y_{n+1} < y_n$); points of the polygon are numbered in the trigonometric sense.

The volume of the torus is just the algebraic sum of the V_n's; hence

$$\mathcal{V}_y = \frac{\pi}{3}\sum_{n=1}^{N}\left(x_n^2 + x_n x_{n+1} + x_{n+1}^2\right)(y_{n+1} - y_n)$$

for a N-point polygon (one assumes $A_{N+1} = A_1$).

Noting that the surface of the polygon is given by

$$S = \frac{1}{2}\sum_{n=1}^{N}(x_n y_{n+1} - x_{n+1} y_n)$$

the result follows.

References

Brandt P.N., Ferguson S., Scharmer G.B., et al., 1991, Variations of granulation properties on a mesogranular scale. A&A 241, 219

Brandt P.N., Scharmer G.B., Ferguson S., et al., 1988 Vortex flow in the solar photosphere. Nat 335, 238

Darvann T.A., 1991, Solar horizontal flows and differential rotation determined by local correlation tracking of granulation. Ph.D. Thesis, Oslo University

Kitai R., Funakoshi Y., Ueno S., Sano S., Ichimoto K., 1997, Real-time frame selector and its application to observations of the horizontal velocity field in the solar photosphere. PASJ 49, 513

Mehltretter J.P., 1978, Balloon-borne imagery of the solar granulation. II. the lifetime of solar granulation. A&A 62, 311

Molowny Horas R.L., 1994, Dynamics and structure of the solar Chromosphere. Ph.D. Thesis, Oslo University

Muller R., Auffret H., Roudier T., et al., 1992, Evolution and advection of solar mesogranulation. Nat 356, 322

November L., 1986, Measurement of geometric distortion in a turbulent atmosphere. J. Appl. Optics 25, 392

November L., 1989, Proper motion measurements of solar granulation: the case for mesogranulation. In: Von der Lühe O. (ed.) High Spatial Resolution Observations. p. 457

November L.J., Simon G.W., 1988, Precise proper-motion measurement of solar granulation. AJ 333, 427

Pérez J.-Ph., 1997, Mécanique. Masson

Roudier T., Muller R., 1986, Structure of the solar granulation. Solar Phys. 107, 11

Roudier T., Malherbe J.-M., Vigneau J., Pfeiffer B., 1998, Solar mesogranule lifetime measurements. A&A 330, 1136

Simon G.W., Brandt P.N., November L., Scharmer G.B., Shine R.A., 1994, Large-scale photospheric motions: first results from an extraordinary eleven-hour granulation observation. In: Rutten R.J., Schriver C.J. (eds.)Solar surface Magnetism. Kluwer Ac. Publ.

Simon G.W., Brandt P.N., November L., Shine R., Strous L.H., 1995 Warning: local correlation tracking may be dangerous to your (scientific) health. In: Proc. of 4th SOHO Workshop: Helioseismology. ESA SP-376, p. 223

Straus T., Bonaccini D., 1997, Dynamics of the solar photosphere I. Two-dimensional spectroscopy of mesoscale phenomena. A&A 324, 704

Strous L., 1994, Dynamics in Solar Active Regions: Patterns in Magnetic-flux Emergence. Ph.D. Thesis, University of Utrecht

Strous L., 1995a, Feature tracking: deriving horizontal motion and more. In: Proc. of 4th SOHO Workshop: Helioseismology. ESA SP-376, p. 213

Strous L., 1995b, Comparison of flow maps derived by various techniques. In Proc. of 4th SOHO Workshop: Helioseismology. ESA SP-376, p. 219

Title A., Tarbell T., Topka K., Ferguson S., Shine R., 1989, Statistical properties of solar granulation derived from the SOUP instrument on spacelab 2. AJ 336, 475

Torrence C., Compo G.P., 1998, A practical guide to wavelet analysis. Bull. of Am. Meteo. Soc. 79, 61

Ueno S., Kitai R., 1998, 3D velocity-field observation of solar convection. I. Characteristics of mesogranulation. PASJ 50, 125

Wang Y., Noyes R., Tarbell T., Title A., 1995, Vorticity and divergence in the solar photosphere. AJ 447, 419